Active

Project #: E-16-N54 Cost share #: Rev #: 0
Center # : 10/24-6-R0284-0A0 Center shr #: OCA file #:
Work type : RES
Contract#: 880400680 Mod #: INITIATION Document : AGR
Prime #: Contract entity: GTRC

Subprojects ? : N CFDA: N/A
Main project #: PE #: N/A

Project unit: AERO ENGR Unit code: 02.010.110
Project director(s):
SANKAR N L AERO ENGR (404)894-3014
SMITH M J AERO (404)-

Sponsor/division names: LOCKHEED/MARTIN / ORLANDO, FL
Sponsor/division codes: 211 / 053

Award period: 970127 to 970327 (performance) 970327 (reports)

Sponsor amount	New this change	Total to date
Contract value	19,914.00	19,914.00
Funded	19,914.00	19,914.00
Cost sharing amount		0.00

Does subcontracting plan apply ?: N

Title: COMPUTATIONAL ANALYSIS OF AERO. LOADS ON P3 PATORAL AIRCRAFT TURRET SENSOR...

PROJECT ADMINISTRATION DATA

OCA contact: Michelle A. Starmack 894-4820

Sponsor technical contact

GEORGE GO, MAIL POINT 040
(407)356-2147

LOCKHEED MARTIN CORPORATION
ELECTRONICS & MISSILES
5600 SNAD LAKE ROAD
ORLANDO, FL 32819-8907

Sponsor issuing office

BEVERLY WORTHAM-HUDGINS, MP 126
(407)356-2147

LOCKHEED MARTIN
ELECTRONICS AND MISSILES
5600 SAND LAKE ROAD
ORLANDO, FL 32819-8907
FAX (407) 356-1380

Security class (U,C,S,TS) : U ONR resident rep. is ACO (Y/N): N
Defense priority rating : N/A N/A supplemental sheet
Equipment title vests with: Sponsor X GIT
NO EQUIPMENT PROPOSED
Administrative comments -
INITIATION OF PROJECT.

GEORGIA INSTITUTE OF TECHNOLOGY
OFFICE OF CONTRACT ADMINISTRATION

NOTICE OF PROJECT CLOSEOUT

4

E-16-N54

Closeout Notice Date 04/10/97

Project No. E-16-N54 Center No. 10/24-6-R0284-0A0

Project Director SANKAR N L School/Lab AERO ENGR

Sponsor LOCKHEED/MARTIN/ORLANDO, FL

Contract/Grant No. 880400680 Contract Entity GTRC

Prime Contract No.

Title COMPUTATIONAL ANALYSIS OF AERO. LOADS ON P3 PATORAL AIRCRAFT TURRET SENSO

Effective Completion Date 970327 (Performance) 970327 (Reports)

Closeout Actions Required:	Y/N	Date Submitted
Final Invoice or Copy of Final Invoice	Y	
Final Report of Inventions and/or Subcontracts	N	
Government Property Inventory & Related Certificate	N	
Classified Material Certificate	N	
Release and Assignment	N	
Other	N	

Comments

Subproject Under Main Project No.

Continues Project No.

Distribution Required:

Project Director	Y
Administrative Network Representative	Y
GTRI Accounting/Grants and Contracts	Y
Procurement/Supply Services	Y
Research Property Managment	Y
Research Security Services	N
Reports Coordinator (OCA)	Y
GTRC	Y
Project File	Y
Other	N
	N

COMPUTATIONAL ANALYSIS OF AERODYNAMIC LOADS ON P3 PATROL AIRCRAFT TURRET SYSTEM

Final report

Submitted to

Lockheed Martin Electronics & Missiles
Attn: George Go
Mail Point 126
5600 Sand Lake Road
Orlando, FL 32819

Prepared by

Lakshmi N. Sankar
Regents' Professor

Marilyn Smith
Adjunct Professor

Stephen L. Quackenbush and Anurag Gupta
Graduate Research Assistants

School of Aerospace Engineering
Atlanta, GA 30332-0150

March 1997

TABLE OF CONTENTS

I. INTRODUCTION

This research deals with the calculation of airloads on two sensors used on the P-3 patrol aircraft. The first sensor, in use on operational aircraft is referred to as the baseline configuration in this report. The second sensor, being evaluated by Lockheed Martin, is referred to in this document as the "new configuration."

The configurations were supplied to Georgia Tech as CAD files which may be opened using programs such as IDEAS. The new configuration differs from the baseline configuration in a number of ways. There are flat, faceted mirrors on the new configuration. The post on which the sensor is placed has relatively sharp edges. It is anticipated that significant flow separation may occur at the corners of these posts, and at the edges of the mirrors. The objective of this research is to determine how the loads on the new configuration deviate from the original configuration. The pitching, rolling and yawing moments on the post were also considered, since these moments are transmitted to the aircraft. The pitching, rolling and yawing moments of the sensor (i.e. spherical portion of the configuration) are also important, because these moments should be overcome by resistive moments generated by motors that turn and position the mirrors. In the absence of the resistive moments, the unconstrained sensor will begin to windmill.

Two flight conditions (200 knots and 400 knots), three cross flow conditions ($\pm$ 45 degrees and zero yaw), two mirror azimuth locations (0 degrees, -10 degrees and -45 degrees) were considered in this study. This represents a total combination of 36 conditions (two sensors; two Mach numbers; three yaw angles; three azimuth locations). Fortunately these calculations could be reduced to a smaller subset as a result of a number of assumptions, verified by calculations. For example,

i) the calculations revealed that the flow was subsonic at the 200 knot condition, and no compressibility effects were observed. As a result, the loads at the higher speed (400 knots) could be extrapolated from the lower speed simply by scaling the dynamic pressure by a factor of 4.
ii) Secondly, for the baseline sensor, calculations with and without the fuselage surface showed the fuselage to have little effect on the airloads. This was due to the fact that the curvature of the fuselage surface was very small, compared to the sensor. Since the baseline sensor was axially symmetric, the loads were independent of yaw angle, and azimuth angle of the spherical portion of the sensor.
iii) Finally, calculations for the new configuration with and without the mirrors showed that the presence of mirrors for the new configuration affected the airloads only slightly. Therefore, only a subset of the 18 calculations for the second configuration had to be carried out.

All the flow calculations were done using the NASA Langley computer code called GASP. The body-fitted grids over these configurations were done

using a public domain computer code called GRIDGEN. An independent analysis with a flow solver called ENS3D was also carried out in some instances, to ensure that the choice of a flow solver does not dramatically change the airloads predicted. In all, seven calculations were done for the two configurations, and are discussed in detail in this report.

The rest of this document is organized as follows. The original statement of work is included in the next section. A separate section deals with the mathematical formulation behind the flow solvers FAST and ENS3D. Next, the results from the analyses are discussed, pointing out the geometric features that give rise to variations in the pressure field, and hence the airloads on the sensors. A list of conclusions is given at the end of this report.

II. Statement of Work

Computational Analysis of Aerodynamic Loads on the P-3 Patrol Aircraft Turret Sensor System

In this section, the original statement of work prepared at the time the contract was awarded is given.

Introduction

The P-3 patrol aircraft utilizes a turret sensor system mounted on the centerline of the lower-forward fuselage, aft of the radome. The turret system approximates a right circular cylinder capped with a hemisphere. A geometrically similar, modified turret system has also been proposed for the P-3. For either configuration, it is critical that the aerodynamic forces be known for design purposes. For the proposed system, this is particularly true as the turret is capable of rotating continuously 360 degrees in azimuth, and +20/-120 degrees in elevation. In particular, the power or torque required to overcome the weather vane effect must be known.

Objectives

The objective of this proposal is to perform computational fluid dynamics analyses to determine the aerodynamic loads on the current and proposed turret system of the P-3 aircraft. Computed loads (forces and moments) will provide insight into structural and torque design requirements.

Approach

The minimize the cost and duration of time, the analysis will make use of preexisting surface definitions of the fuselage and the turret system, supplied by Lockheed Martin to the researchers. The grid generation and the flow analyses will be done using a family of computer codes developed CFD Research Corporation, and the Wright Laboratories.

The computer codes GRIDGEN or CFD-GEOM-UN will be used to generate the body-fitted grid around the lower fuselage, and the turret system. This analysis can generate structured grids that divide the flow field into deformed brick-like elements. For a regular, smooth geometry structured grids work best. If the geometry is irregular, and has sharp corners, an unstructured grid which divides the flow field into a collection of tetrahedra may be necessary. The CFD-GEOM-UN solver can develop both these types of grids.

The flow analysis will be done by a suite of CFD codes called GASP, CFD-ACE and COBALT. The CFD-ACE and GASP analyses have a graphical user interface, permitting easy, intuitive interaction with the analysis. This solver can handle structured or unstructured grids. The effects of turbulence is modeled using a k-e turbulence model. The CFD-ACE and GASP codes are best suited for low speed, incompressible flows. The COBALT code is suitable for high subsonic and transonic flows.

Work Plan

1. Geometry Definition and grid generation: Existing IGES files and fuselage definition will be acquired from the sponsor. Body fitted grids, which contain 100,000 to 150,000 elements (structured or unstructured) will be generated.

2. Flow Analysis: Analyses will be carried out for the following parameters:
   Azimuth Angle: Design, + 45° and -45°
   Elevation Angle: Design Angle, +10°, -45°
   Airspeed: 200 and 400 knots.
   Angle of Attack: 3°

If each of these parameters will be individually varied, holding the others fixed, a total of 36 analyses will be needed. It is suggested that approximately 12 analyses be done bracketing the above flight regimes.

3. Presentation of Results: The researchers will meet with the sponsor at least twice during the research period to brief the sponsor on interim results obtained. A final report summarizing the results for all tasks performed will also be prepared. This report will detail all force and moment calculations, and include pictures of flow field indicating separated flow patterns.

Work schedule

1. Geometry definition and Grid Generation will be done during the first two weeks of the effort.

2. The flow analysis will begin during week 3, and run through week 7.

3. The final report preparation will begin on week 7, and end by week 8.

Key personnel

Prof. L. N. Sankar, Regents' Professor, School of Aerospace Engineering, Georgia Tech, Project Principal Investigator

Dr. Marilyn Smith, Adjunct Professor, School of Aerospace Engineering, Georgia Tech, Project Co-Principal Investigator

Proposed starting date

A starting date of December 23, 1996 is requested. Final report will be completed by February 23, 1997.

III. MATHEMATICAL FORMULATION BEHIND THE FLOW SOLVERS

The flow solvers ENS3D and GASP were used in this study. At the time the proposal was written, other flow solvers such as COBALT had been acquired, or were available in house. It was found that both the configurations could be analyzed using a single solver GASP, with the ENS3D providing valuable cross check.

Both these flow solvers solve the governing equations, known as Navier-Stokes equations on an irregular, body-fitted grid surrounding the geometry. Samples of such grids will be shown in the section on results and discussions. Because it is difficult to do analytical operations such as differentiation, interpolation etc. directly on a curvilinear grid, this grid is mapped onto a regular brick-like coordinate system (ξ,η,ζ), called the transformed coordinate system.

Mathematical Formulation

The vector form of the full Reynolds-averaged, 3-D Navier-Stokes equations based can be written as:

$$\mathbf{Q}_\tau + \mathbf{E}_\xi + \mathbf{F}_\eta + \mathbf{G}_\zeta = \mathbf{R}_\xi + \mathbf{S}_\eta + \mathbf{T}_\zeta \tag{1}$$

where **Q** is the vector of unknown flow properties; **E**, **F**, **G** are the inviscid flux vectors; and **R**, **S**, **T** are the viscous flux vectors. Eq. (1) may be written in non-dimensional form, using as non-dimensionalization quantities ρ_∞ for density, a_∞ for velocity, c (reference chord) for length, μ_∞ for viscosity, and $\rho_\infty a_\infty^2$ for pressure, as:

$$\mathbf{Q}_\tau + \mathbf{E}_\xi + \mathbf{F}_\eta + \mathbf{G}_\zeta = \frac{1}{\mathrm{Re}}\left(\mathbf{R}_\xi + \mathbf{S}_\eta + \mathbf{T}_\zeta\right) \tag{2}$$

where $\mathrm{Re} = \rho_\infty a_\infty c/\mu_\infty$ is the Reynolds number based on the free-stream speed of sound. The resulting non-dimensional flux vectors are:

$$\mathbf{Q} = \frac{1}{J}\begin{Bmatrix} \rho \\ \rho u \\ \rho v \\ \rho w \\ e \end{Bmatrix} \quad ; \quad \mathbf{E} = \frac{1}{J}\begin{Bmatrix} \rho U \\ \rho u U + \xi_x p \\ \rho v U + \xi_y p \\ \rho w U + \xi_z p \\ (e+p)U - \xi_t p \end{Bmatrix} \quad ; \quad \mathbf{F} = \frac{1}{J}\begin{Bmatrix} \rho V \\ \rho u V + \eta_x p \\ \rho v V + \eta_y p \\ \rho w V + \eta_z p \\ (e+p)V - \eta_t p \end{Bmatrix};$$

$$\mathbf{G}=\frac{1}{J}\begin{Bmatrix}\rho W\\ \rho uW+\zeta_x p\\ \rho vW+\zeta_y p\\ \rho wW+\zeta_z p\\ (e+p)W-\zeta_t p\end{Bmatrix};\qquad \mathbf{R}=\frac{1}{J}\begin{Bmatrix}0\\ \xi_x\tau_{xx}+\xi_y\tau_{xy}+\xi_z\tau_{xz}\\ \xi_x\tau_{xy}+\xi_y\tau_{yy}+\xi_z\tau_{yz}\\ \xi_x\tau_{xz}+\xi_y\tau_{yz}+\xi_z\tau_{zz}\\ \xi_x R_5+\xi_y S_5+\xi_z T_5\end{Bmatrix};$$

$$\mathbf{S}=\frac{1}{J}\begin{Bmatrix}0\\ \eta_x\tau_{xx}+\eta_y\tau_{xy}+\eta_z\tau_{xz}\\ \eta_x\tau_{xy}+\eta_y\tau_{yy}+\eta_z\tau_{yz}\\ \eta_x\tau_{xz}+\eta_y\tau_{yz}+\eta_z\tau_{zz}\\ \eta_x R_5+\eta_y S_5+\eta_z T_5\end{Bmatrix};\qquad \mathbf{T}=\frac{1}{J}\begin{Bmatrix}0\\ \zeta_x\tau_{xx}+\zeta_y\tau_{xy}+\zeta_z\tau_{xz}\\ \zeta_x\tau_{xy}+\zeta_y\tau_{yy}+\zeta_z\tau_{yz}\\ \zeta_x\tau_{xz}+\zeta_y\tau_{yz}+\zeta_z\tau_{zz}\\ \zeta_x R_5+\zeta_y S_5+\zeta_z T_5\end{Bmatrix} \tag{3}$$

where J is the Jacobian of the transformation between Cartesian and curvilinear coordinates, given by:

$$J=\left[y_\xi(x_\zeta z_\eta-x_\eta z_\zeta)+y_\eta(x_\xi z_\zeta-x_\zeta z_\xi)+y_\zeta(x_\eta z_\xi-x_\xi z_\eta)\right]^{-1} \tag{4}$$

U, V and W are the contravariant components of velocity, given by:

$$\begin{aligned}U&=\xi_t+\xi_x u+\xi_y v+\xi_z w\\ V&=\eta_t+\eta_x u+\eta_y v+\eta_z w\\ W&=\zeta_t+\zeta_x u+\zeta_y v+\zeta_z w\end{aligned} \tag{5}$$

The pressure p is related to the total energy per unit volume e and kinetic energy per unit volume by:

$$p=(\gamma-1)\left[e-\frac{1}{2}\rho(u^2+v^2+w^2)\right] \tag{6}$$

The shear stresses are given by:

$$
\begin{aligned}
\tau_{xx} &= \mu\left[\frac{4}{3}\left(u_\xi \xi_x + u_\eta \eta_x + u_\zeta \zeta_x\right) - \frac{2}{3}\left(v_\xi \xi_y + v_\eta \eta_y + v_\zeta \zeta_y + w_\xi \xi_z + w_\eta \eta_z + w_\zeta \zeta_z\right)\right] \\
\tau_{xy} &= \mu\left[\left(u_\xi \xi_y + u_\eta \eta_y + u_\zeta \zeta_y\right) + \left(v_\xi \xi_x + v_\eta \eta_x + v_\zeta \zeta_x\right)\right] \\
\tau_{xz} &= \mu\left[\left(u_\xi \xi_z + u_\eta \eta_z + u_\zeta \zeta_z\right) + \left(w_\xi \xi_x + w_\eta \eta_x + w_\zeta \zeta_x\right)\right] \\
\tau_{yy} &= \mu\left[\frac{4}{3}\left(v_\xi \xi_y + v_\eta \eta_y + v_\zeta \zeta_y\right) - \frac{2}{3}\left(u_\xi \xi_x + u_\eta \eta_x + u_\zeta \zeta_x + w_\xi \xi_z + w_\eta \eta_z + w_\zeta \zeta_z\right)\right] \\
\tau_{yz} &= \mu\left[\left(v_\xi \xi_z + v_\eta \eta_z + v_\zeta \zeta_z\right) + \left(w_\xi \xi_y + w_\eta \eta_y + w_\zeta \zeta_y\right)\right] \\
\tau_{zz} &= \mu\left[\frac{4}{3}\left(w_\xi \xi_z + w_\eta \eta_z + w_\zeta \zeta_z\right) - \frac{2}{3}\left(u_\xi \xi_x + u_\eta \eta_x + u_\zeta \zeta_x + v_\xi \xi_y + v_\eta \eta_y + v_\zeta \zeta_y\right)\right]
\end{aligned}
\tag{7}
$$

and

$$
\begin{aligned}
R_5 &= u\tau_{xx} + v\tau_{xy} + w\tau_{xz} + \frac{\mu}{\Pr(\gamma - 1)}\left(\xi_x \frac{\partial a^2}{\partial \xi} + \eta_x \frac{\partial a^2}{\partial \eta} + \zeta_x \frac{\partial a^2}{\partial \zeta}\right) \\
S_5 &= u\tau_{xy} + v\tau_{yy} + w\tau_{yz} + \frac{\mu}{\Pr(\gamma - 1)}\left(\xi_y \frac{\partial a^2}{\partial \xi} + \eta_y \frac{\partial a^2}{\partial \eta} + \zeta_y \frac{\partial a^2}{\partial \zeta}\right) \\
T_5 &= u\tau_{xz} + v\tau_{yz} + w\tau_{zz} + \frac{\mu}{\Pr(\gamma - 1)}\left(\xi_z \frac{\partial a^2}{\partial \xi} + \eta_z \frac{\partial a^2}{\partial \eta} + \zeta_z \frac{\partial a^2}{\partial \zeta}\right)
\end{aligned}
\tag{8}
$$

where $\Pr = \mu c_p / k$ is the Prandtl number and a is the speed of sound.

In turbulent flows, the molecular viscosity μ appearing in Eqs. (7) and (8) is replaced by $\mu + \mu_T$, and the quantity $\mu/\Pr$ in Eq. (2.8) is replaced by $\mu/\Pr + \mu_T/\Pr_T$, where μ_T is an eddy viscosity and $\Pr_T$ is the turbulent Prandtl number.

Numerical Formulation

In this section the finite-difference numerical formulation of the Navier-Stokes equations (2) is discussed. First, the finite-difference discretization of the derivatives is described. Next, the linearization of the resulting non-linear system of equations and its approximate factorization into an LU systems of equations are discussed. Finally the numerical implementation is described.

Discretization

The time derivative, $\mathbf{Q}_\tau$, of equation (2) is approximated using two-point backward difference at the new time level 'n+1':

$$\mathbf{Q}_\tau = \frac{\mathbf{Q}^{n+1} - \mathbf{Q}^n}{\Delta\tau} + O(\Delta\tau) = \frac{\Delta\mathbf{Q}^{n+1}}{\Delta\tau} + O(\Delta\tau) \tag{9}$$

where 'n' refers to the time level at which all quantities are known, and 'n+1' is the new time level. All spatial derivatives are approximated by standard second-order central differences and are represented by the difference operators δ , e.g.:

$$(\mathbf{E}_\xi)_{i,j,k} = (\delta_\xi \mathbf{E})_{i,j,k} + O(\Delta\xi^2) = \frac{\mathbf{E}_{i+1,j,k} - \mathbf{E}_{i-1,j,k}}{2\Delta\xi} + O(\Delta\xi^2) \tag{10}$$

Note that the choice of $\Delta\xi = \Delta\eta = \Delta\zeta = 1$ in the computational space is made for convenience.

The spatial derivatives, $\mathbf{E}\xi$ and $\mathbf{G}\zeta$ etc. are evaluated implicitly at the new time level 'n+1'.

$$\frac{\mathbf{Q}^{n+1}_{i,j,k} - \mathbf{Q}^{n}_{i,j,k}}{\Delta\tau} + \frac{\mathbf{E}^{n+1}_{i+1,j,k} - \mathbf{E}^{n+1}_{i-1,j,k}}{2} + \frac{\mathbf{F}^{n+1}_{i,j+1,k} - \mathbf{F}^{n+1}_{i,j-1,k}}{2} + \frac{\mathbf{G}^{n+1}_{i,j,k+1} - \mathbf{G}^{n+1}_{i,j,k-1}}{2} \tag{11}$$

The viscous terms $\mathbf{R}\xi$, $\mathbf{S}\eta$ and $\mathbf{T}\zeta$ are evaluated explicitly, using half-point central differences denoted here by the difference operator $\bar{\delta}$, so that the computational stencil for the stress terms uses only three nodes in each of the three directions. For example, in the computation of $\mathbf{R}_\xi$, the term $\left(\xi_x^2 \mu u_\xi\right)_\xi$ appears and is discretized as follows:

$$\left(\xi_x^2 \mu u_\xi\right)_\xi = \bar{\delta}\left(\xi_x^2 \mu u_\xi\right) + O(\Delta\xi^2) = \frac{\left(\xi_x^2 \mu u_\xi\right)_{i+1/2,j,k} - \left(\xi_x^2 \mu u_\xi\right)_{i-1/2,j,k}}{\Delta\xi} + O(\Delta\xi^2)$$

$$\approx \frac{\left(\xi_x^2 \mu\right)_{i+1/2,j,k} \dfrac{u_{i+1,j,k} - u_{i,j,k}}{\Delta\xi} - \left(\xi_x^2 \mu\right)_{i-1/2,j,k} \dfrac{u_{i,j,k} - u_{i-1,j,k}}{\Delta\xi}}{\Delta\xi}$$

$$\approx \frac{\dfrac{\left(\xi_x^2 \mu\right)_{i,j,k} + \left(\xi_x^2 \mu\right)_{i+1,j,k}}{2} \dfrac{(u_{i+1,j,k} - u_{i,j,k})}{\Delta\xi} - \dfrac{\left(\xi_x^2 \mu\right)_{i,j,k} + \left(\xi_x^2 \mu\right)_{i-1,j,k}}{2} \dfrac{(u_{i,j,k} - u_{i-1,j,k})}{\Delta\xi}}{\Delta\xi} \tag{13}$$

$$= \frac{1}{2}\left\{\left[\left(\xi_x^2 \mu\right)_{i,j,k} + \left(\xi_x^2 \mu\right)_{i+1,j,k}\right](u_{i+1,j,k} - u_{i,j,k}) - \left[\left(\xi_x^2 \mu\right)_{i,j,k} + \left(\xi_x^2 \mu\right)_{i-1,j,k}\right](u_{i,j,k} - u_{i-1,j,k})\right\}$$

Explicit treatment of the stress terms still permits the use of large time steps since the Reynolds numbers of interest here are fairly large.

With the above described time and space discretizations, the discretized form of Eq. (2) becomes:

$$\Delta\mathbf{Q}^{n+1} = -\Delta\tau\left(\delta_\xi \mathbf{E}^{n+1} + \delta_\eta \mathbf{F}^{n+1} + \delta_\zeta \mathbf{G}^{n+1}\right) + \frac{\Delta\tau}{\mathrm{Re}}\left(\bar{\delta}_\xi \mathbf{R}^n + \bar{\delta}_\eta \mathbf{S}^n + \bar{\delta}_\zeta \mathbf{T}^n\right) \tag{14}$$

Linearization

The time and space discretizations described above lead to a system of non-linear, block hepta-diagonal matrix equations for the unknown $\Delta\mathbf{Q}^{n+1} = \mathbf{Q}^{n+1} - \mathbf{Q}^n$, Eq. (14), since the convection fluxes **E**, **F**, **G** are non-linear functions of the vector of unknown flow properties **Q**. Equation (2.14) is then linearized using the Jacobian matrices $\mathbf{A} = \partial\mathbf{E}/\partial\mathbf{Q}$ and $\mathbf{C} = \partial\mathbf{G}/\partial\mathbf{Q}$, given by:

$$\begin{pmatrix}\mathbf{A}\\ \text{or}\\ \mathbf{C}\end{pmatrix} = \begin{bmatrix} k_t & k_x & k_y & k_z & 0 \\ k_x\phi^2 - u\theta & \Theta - k_x\gamma_2 u & k_y u - k_x\gamma_1 v & k_z u - k_x\gamma_1 w & k_x\gamma_1 \\ k_y\phi^2 - v\theta & k_x v - k_y\gamma_1 u & \Theta - k_y\gamma_2 v & k_z v - k_y\gamma_1 w & k_y\gamma_1 \\ k_z\phi^2 - w\theta & k_x w - k_z\gamma_1 u & k_y w - k_z\gamma_1 v & \Theta - k_z\gamma_2 w & k_z\gamma_1 \\ \theta\left(\phi^2 - b\right) & k_x b - \gamma_1 u\theta & k_y b - \gamma_1 v\theta & k_z b - \gamma_1 w\theta & k_t + \gamma\theta \end{bmatrix} \tag{15}$$

where:

$$k = \begin{cases}\xi & \text{for } \mathbf{A} \\ \zeta & \text{for } \mathbf{C}\end{cases} \quad ; \quad \phi^2 = \frac{\gamma - 1}{2}\left(u^2 + v^2 + w^2\right) \quad ; \quad \theta = k_x u + k_y v + k_z w \quad ;$$

$$\Theta = k_t + \theta \quad ; \quad \gamma_1 = \gamma - 1 \quad ; \quad \gamma_2 = \gamma - 2 \quad ; \quad b = \frac{\gamma e}{\rho} - \phi^2 \tag{16}$$

The linearization is obtained as follows:

$$\mathbf{E}^{n+1} = \mathbf{E}^n + \underbrace{\left(\frac{\partial\mathbf{E}}{\partial\mathbf{Q}}\right)^n}_{\mathbf{A}^n} \underbrace{\left(\mathbf{Q}^{n+1} - \mathbf{Q}^n\right)}_{\Delta\mathbf{Q}^{n+1}} + O\left(\Delta\tau^2\right) = \mathbf{E}^n + \mathbf{A}^n\,\Delta\mathbf{Q}^{n+1} + O\left(\Delta\tau^2\right) \tag{17}$$

and similarly for $\mathbf{G}^{n+1}$. Applying these linearized flux vectors to Eq. (14) yields a formal system of equations for the unknowns:

$$[M]\{\Delta Q\} = \{RHS \text{ of equation } 14\} \tag{18}$$

Inversion of the Matrix System

Eq. (18) is a system of linear, block hepta-diagonal matrix equations, which is considerably expensive to solve directly. Fortunately, the matrix M may be approximately factored into two an L and a U matrix. The resulting LU system may be solved by Gaussian elimination. The errors incurred by the approximate factorization are of order of the time step Δt. In the steady state, the steady state Navier-Stokes equations, represented by right hand side of equation (17) are satisfied. When this is achieved, the solution is said to be converged.

Turbulence Model

A slightly modified version of the Baldwin-Lomax (B-L) algebraic turbulence model is used, where the maximum shear stress is used instead of the wall shear stress because in the vicinity of separation points, the shear stress values approach zero at the wall.

In this model, two layers are considered; in the inner layer, μ_T is given by:

$$(\mu_T)_{\text{inner layer}} = \rho\, \ell_m^2 |\omega| \tag{19}$$

where $|\omega|$ is the mean vorticity, given by:

$$|\omega| = \sqrt{\left(\frac{\partial w}{\partial y} - \frac{\partial v}{\partial z}\right)^2 + \left(\frac{\partial u}{\partial z} - \frac{\partial w}{\partial x}\right)^2 + \left(\frac{\partial v}{\partial x} - \frac{\partial u}{\partial y}\right)^2} \tag{20}$$

and ℓ_m is the mixing length, given by:

$$\ell_m = \kappa d\left[1 - e^{-d_+/A_+}\right] \tag{21}$$

where $\kappa = 0.41$ is the von Kármán constant, d is the distance from the wall, $A_+ = 26.0$ is the van Driest constant, and

$$d_+ = d\frac{\sqrt{\rho\, \tau_{\max}}}{\mu_\infty} \tag{22}$$

The modification with respect to the original Baldwin-Lomax model is apparent in Eq. (22), where $\tau_{\max}$ is used instead of τ_{wall}.

In the outer layer, μ_T is given by:

$$(\mu_T)_{\text{outer layer}} = Kc\rho c_1 F_w F_k \tag{23}$$

where $K_C = 0.0168$ is Clauser's constant, $c_1 = 1.6$ is an empirical constant, F_w is given by:

$$F_w = \min\left(d_{\max} F_{\max}, 0.25 \frac{d_{\max} U_{\text{dif}}^2}{F_{\max}}\right) \tag{24}$$

where

$$F_{\max} = \max\left(\frac{\ell_m \omega}{\kappa}\right) \tag{25}$$

$$U_{\text{dif}} = \max\left(\sqrt{u^2 + v^2 + w^2}\right) - \min\left(\sqrt{u^2 + v^2 + w^2}\right) \tag{26}$$

and $d_{\max}$ is the distance from the wall where $F_{\max}$ occurs. Also in Eq. (23) F_k is given by:

$$F_k = \frac{1}{1 + 5.5\left(\frac{0.3d}{d_{\max}}\right)^6} \tag{27}$$

The switch between inner and outer zones occurs at the distance d_c, defined as the smallest distance from the wall for which $(\mu_T)_{\text{inner layer}} = (\mu_T)_{\text{outer layer}}$.

Numerical Boundary Conditions

The formulation described above must be complemented by appropriate boundary conditions to be specified along the solid surface and far field boundaries.

Solid Surface Boundary

At the solid surfaces, the density and pressure are computed from the adiabatic wall assumption, which implies that their normal derivative at the solid surface is zero, $\partial p/\partial n = \partial \rho/\partial n = 0$.

The velocities at the surface are computed from the no-slip condition, i.e.

$$u = v = w = 0$$

Far Field Boundaries

The far field boundaries are handled as follows. First, the velocity normal to the boundary is computed. Then, the boundary conditions are imposed depending on whether it is an inflow or outflow and whether it is subsonic or supersonic. In the present study, of course, all the velocities are subsonic. The GASP and ENS3D have several user selected options for handling these boundaries. One commonly used option is discussed below:

- Supersonic outflow: all variables are extrapolated from the interior of the domain;
- Subsonic outflow: the pressure is fixed to be the free-stream value and the other variables are extrapolated;
- Subsonic inflow: the density is extrapolated from the interior of the domain and the other variables are fixed from the free-stream;
- Supersonic inflow: all variables are fixed to be the free-stream values.

IV. RESULTS AND DISCUSSION

In this section, all the calculations done to date are discussed. Because the airloads are summarized as a table at the end of the section, the discussions here focus on the grids used, the flow features observed when a steady state solution is reached, and the pressure field on the body surface.

Case 1: Baseline Configuration with Modeling of Fuselage Surface Curvature

The first set of calculations were for the baseline sensor , with part of the fuselage surface modeled. The calculations were done on a 54 x 60 x 60 grid, which contained roughly 3,240 (54 x 60) points on the sensor surface. The ENS3D flow solver was used. The flight conditions were: 200 knots at 20,000 ft altitude. The angle of attack was assumed to be 3 degrees, with zero cross wind. A sample grid surrounding the sensor is shown below.

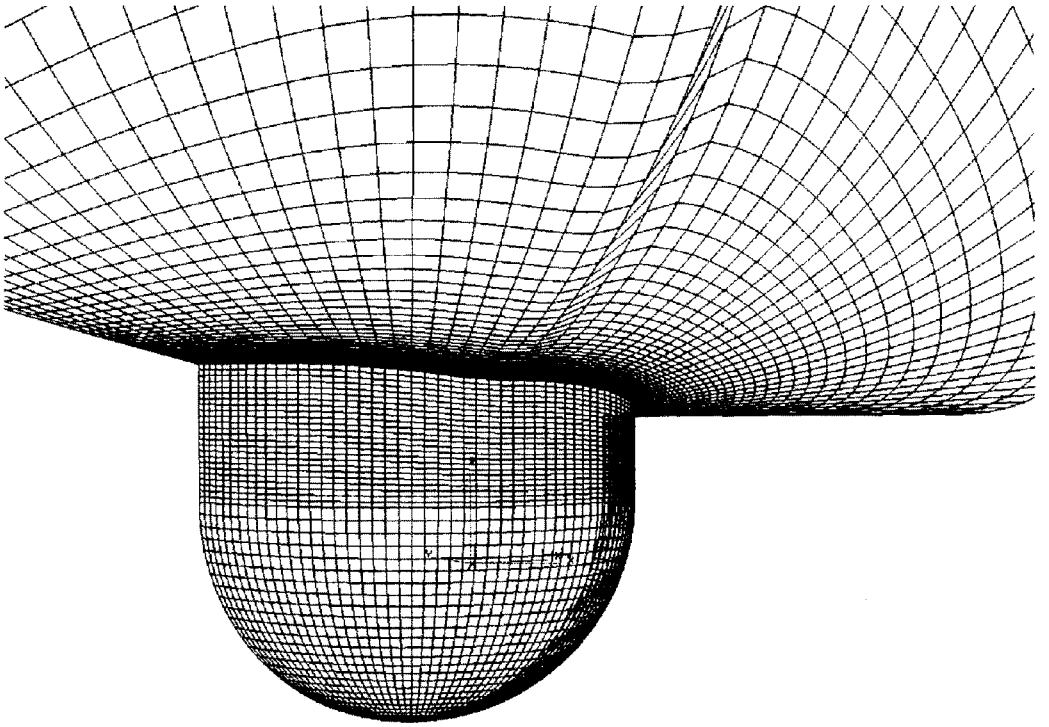

Grid Over Sensor and Fuselage

Figure 1. Surface Grid over the baseline Sensor, Including Fuselage

Figure 2 shows the surface pressure distribution on the front portion of the sensor, and over the fuselage surface. In this figure, the red color represents high pressure regions, the blue represents low pressure region, while green represents pressures close to the freestream value. As may be expected, the flow stagnates in front of the sensor, raising the pressure to high levels, causing a significant drag. Over the shoulders of the

sensor, the flow accelerates rapidly, and the pressure drops below freestream value (blue). The fuselage does not significantly interfere with the flow field, and the pressures over the fuselage remain close to freestream value (green) over most of the surface, except right at the sensor-fuselage interface.

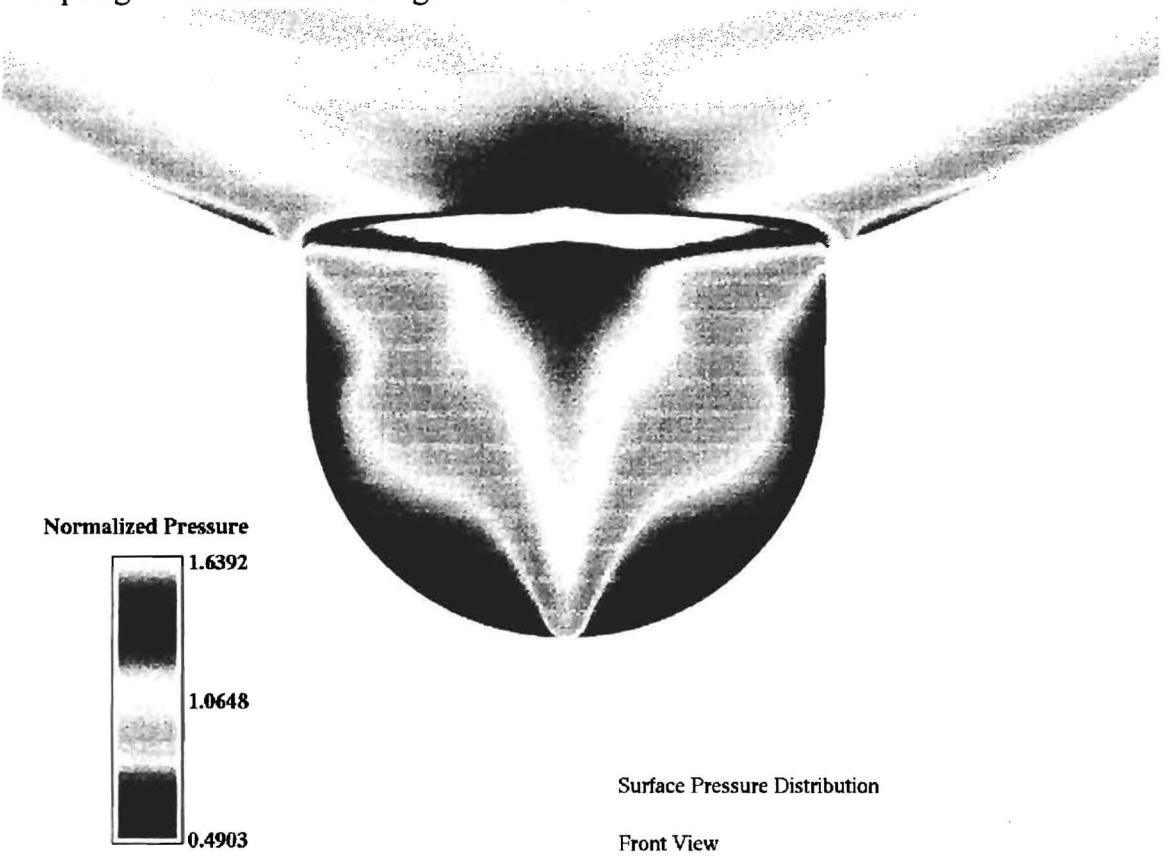

Figure 2. Surface Pressure Distribution over Baseline Sensor - Fuselage Combination (Front View)

Figure 3 shows the pressure field, looking at the sensor from the rear. Again, the pressure over much of the fuselage surface is near freestream value (green). It is seen that some pressure recovery occurs behind the sensor, but stagnation conditions (i.e. high pressures, red) were not established. As stated earlier, the significant pressure difference between the front and the rear of the sensor is the major cause of drag, and pitching moment. Because of the symmetry, no side forces, yawing moment or rolling moment are generated.

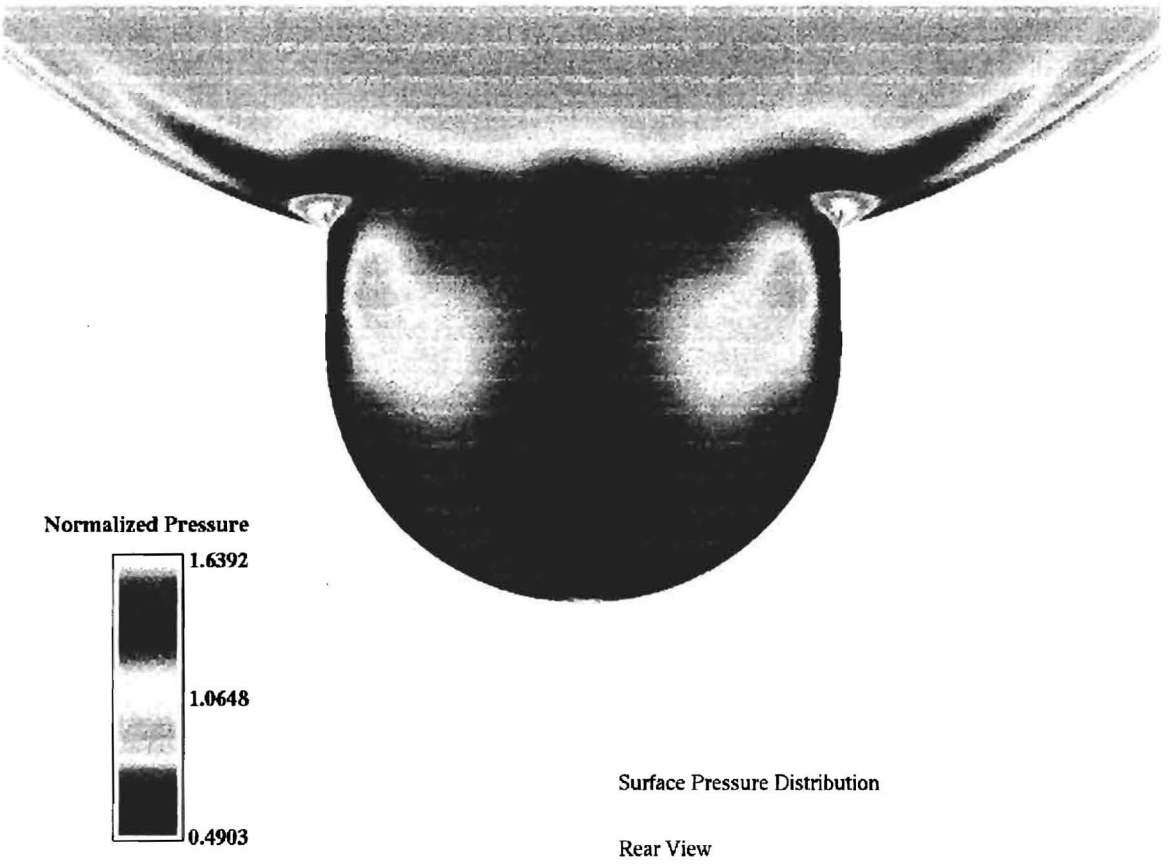

Figure 3. Surface Pressure Distribution over Baseline Sensor - Fuselage Combination (Rear View)

Case 2: Simulation of Baseline Sensor with a Flat Surface representation of the Fuselage

This case is identical to the previous case, except the fuselage surface was modeled as a flat surface, with no fore-aft or lateral curvature. The GASP flow solver was used. The flight conditions were: 200 knots at 20,000 ft altitude. The angle of attack was assumed to be 3 degrees, with zero cross wind. A grid with approximately 3,600 points on the sensor was used.

Figure 4 shows the pressure field over the sensor, with red representing high pressures and blue representing low pressures. The grid as well as some streamlines over the sensor are shown. The flow was fully separated, as in the ENS3D analysis, behind the sphere. The high pressures in front of the sensor, with the low pressure recovery behind leads to a significant amount of drag and pitching moment.

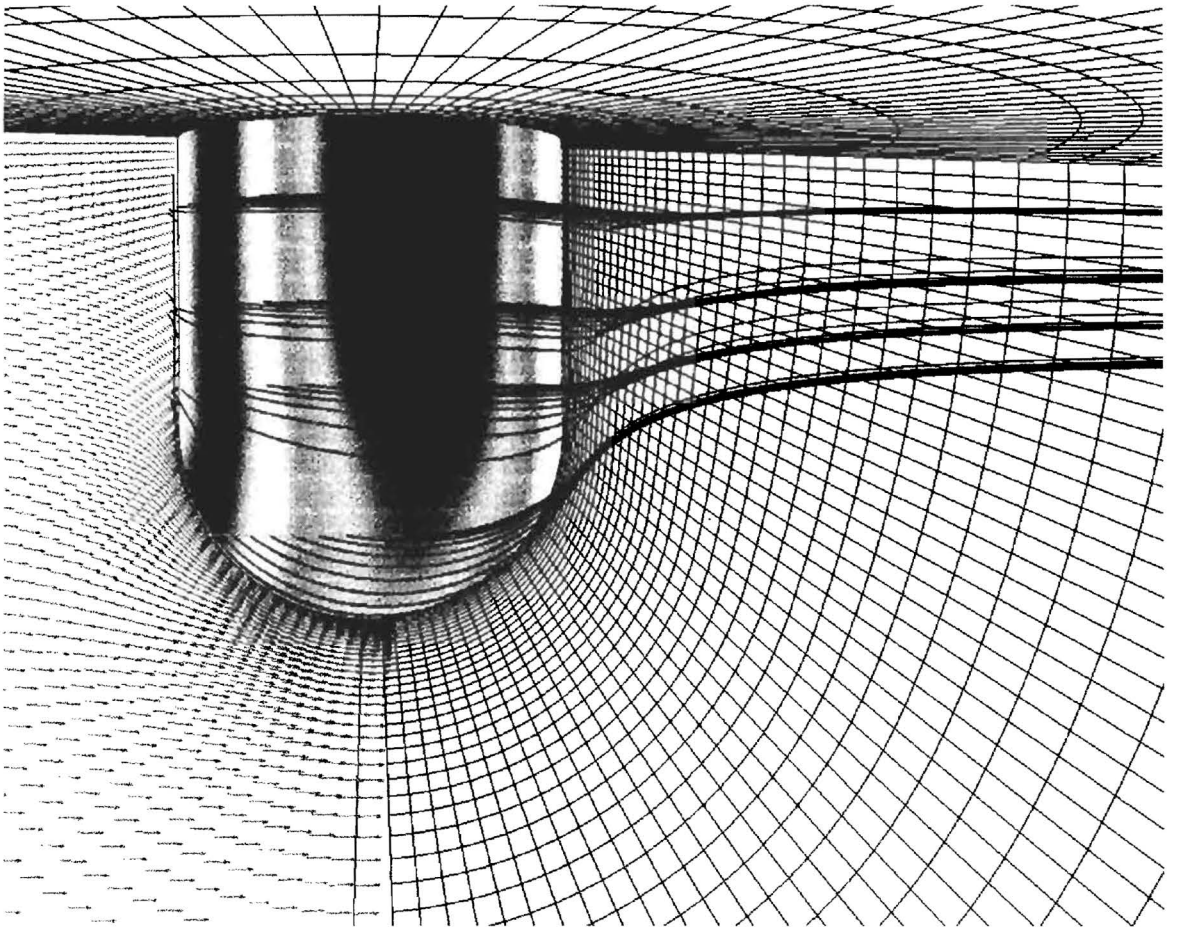

Figure 4. Surface Pressure Distribution and Grid over Baseline Sensor - Flat Fuselage Combination (Side View)

The forces and moments on the sensor are included in Table I. The following observations may be made:

a) The two flow solvers give loads within 25% of each other (e.g. 175 lbf drag for case 2 vs. 218 lbf for case 1.) , despite the fact that widely different grids were used, and that the fuselage surface was modeled only in one of these analysis.
b) Both the solvers predict pressure distributions that are virtually identical, including features such as
    i) strong stagnation pressures on the windward side, and at the base of the post,
    ii) strong suction pressures (i.e. pressures below ambient pressures) over the shoulders of the sensor,
    iii) mild pressure recovery behind the sensor on the leeward side,
    iv) extended separated flow in the wake.

From these similarities it was decided to use the more robust of these flow solvers, GASP, for all subsequent analyses, and to model the fuselage surface as a flat surface. This decision to model the fuselage as a flat surface simplified the grid generation, and allowed concentration of the grid points around the sensor.

Case 3: Simulation of the new Sensor without Mirrors, Zero Yaw

Next, calculations were carried out for the new configuration at zero yaw. The GASP code was used. All the details of the configuration, including the post (made of 4 curved surfaces, the spherical sensor, the interface between the sensor and the post, etc.) were modeled. The only variations between this configuration and the actual configuration were the mirrors, and the fuselage surface curvature. It was believed that a calculation with and without mirrors will be helpful in assessing the effects of the mirrors on the airloads.

Figure 5 below shows the pressure distribution for a typical run - 200 knots, 3 dgerees angle of attack, 20,000 feet altitude. In the figure below, the pink color represents higher than atmospheric pressures, red represents near atmospheric pressure, and green represents pressures below atmosphere. As expected, the windward side has high prressures. The pressure on the fuselage gradually begins to rise upstream of the sensor as the flow approaches the sensor/post. The sides of the post and the bottom of the sensor represent areas of high velocity, and low pressure; these regions are as expected colored in green. The loads for this configuration are given in Table I.

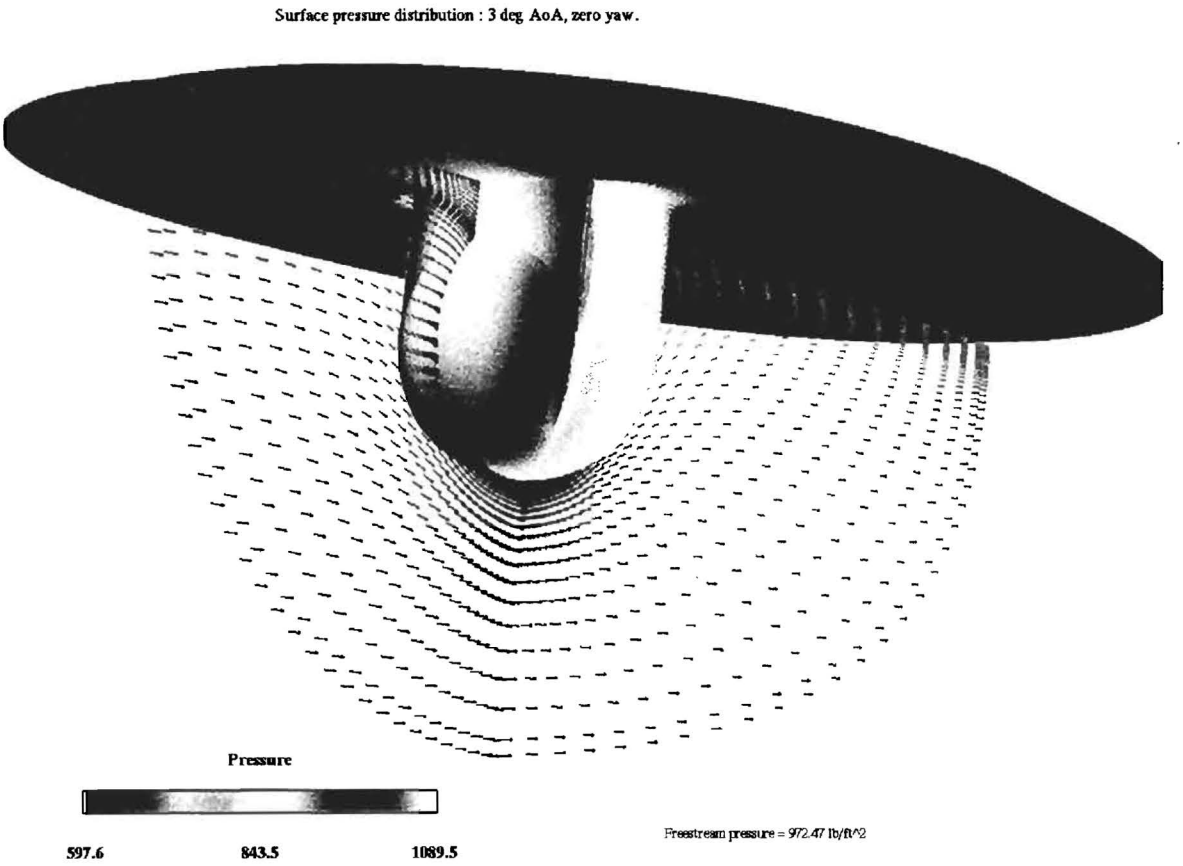

Figure 5. Surface Pressure Distribution and grid over New Sensor - Flat Fuselage Combination, Zero yaw (Perspective View)

Case 4. Simulation of the new Sensor without Mirrors, 45 degree Yaw

This case was identical to the previous case, except the flow was assumed to be at 45 degrees, representing a significant cross wind with reference to the sensor. In the figures below, the surface pressure distribution are shown.

Several features are observed. Part of the sensor, the front portion of the post, and one of the side post are in the windward side, and experience high pressures (purple). At one of the edges of the post, as the flow turns and accelerates, high velocity and low pressures are experienced. Finally, some recovery of the pressure from the low pressures back to near atmospheric pressures (brown) is visible in the leeward side of the sensor.

The cross wind produces significant drag as well as a side force. These forces, and the accompanying moments are presented in table I, and are discussed later, in relation to the other configurations tested.

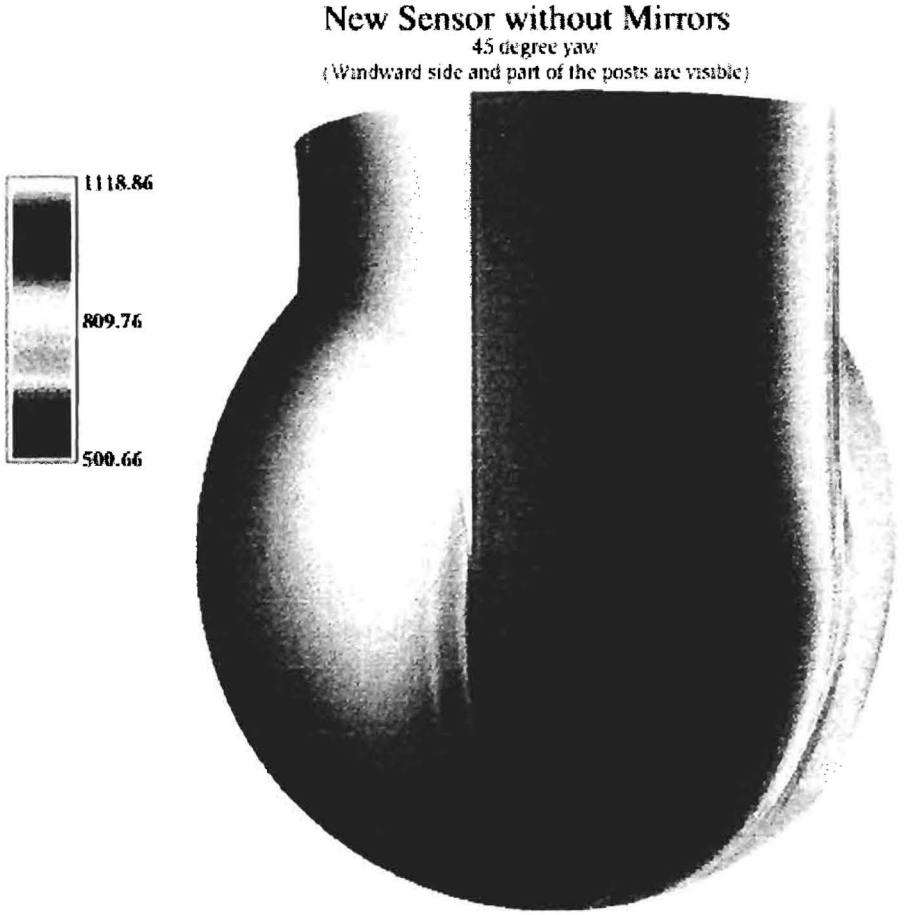

Figure 5. Surface Pressure Distribution and grid over New Sensor - Flat Fuselage Combination, 45 yaw (Perspective View)

Case 5. New sensor with Mirrors, Zero yaw

Next, the new sensor with mirrors is discussed. This configuration was challenging because of the complexity of the mirrors, and the need to position them at the correct spatial location (10 degree azimuth) on the sphere. This was accomplished by a combination of tools:

i) Use of IDEAS to visualize the geometry, and extract the (x,y,z) coordinates on at several points on the mirrors, and post
ii) Development of curve fits for the mirror surfaces (planes, of form ax+by+cz=1) and for the posts (piecewise cylindrical surfaces),
iii) Development of a small computer code to geometrically position the mirrors, sphere and the post,
iv) Development of the grid using GRIDGEN.

The flow solver GASP was able to handle the geometric complexities, and ran without difficulty. The following results shown on figure 6 were obtained for the pressure field, on the windward and leeward sides of the sensor. Many of the expected

features such as stagnation regions, high velocity regions around post corners, pressure recovery to near atmospheric value in the rear were observed. The integrated loads are presented in table I and are discussed later.

New Sensor with Mirrors

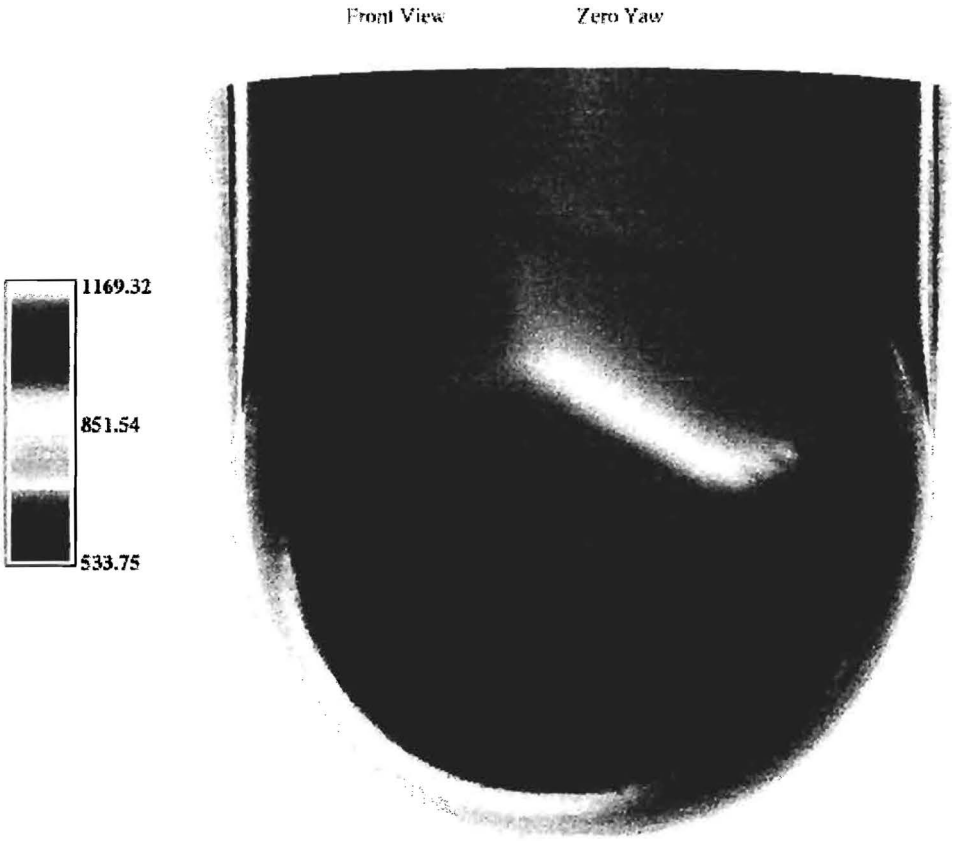

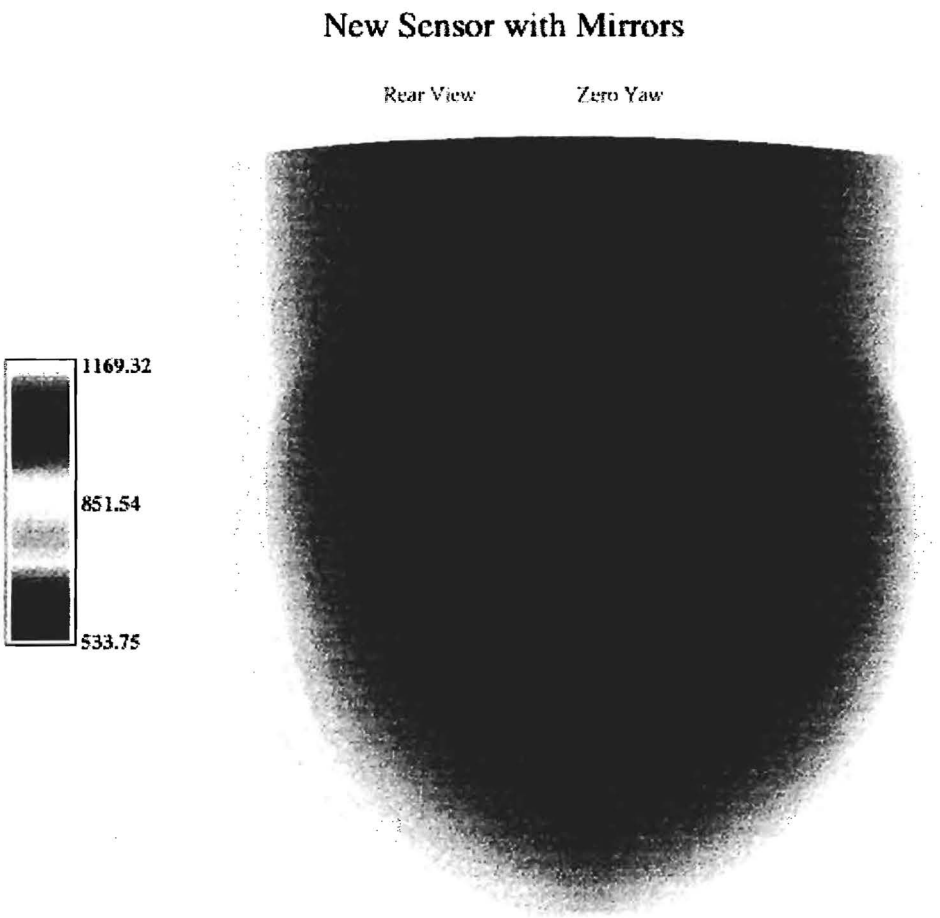

Figure 6. Surface Pressure Distribution over New Sensor with mirrors - Flat Fuselage Combination, Zero yaw (Front and Rear Views)

Case 6: new sensor with Mirrors at 10 degree azimuth, 45 degree yaw

This case was identical to case 5, except the sensor was rotated by 45 degrees, so that it was facing a strong cross wind. The identical tools (IDEAS, GRIDGEN, and GASP) were used, and produced the following results:

New Sensor with Mirrors

45 degrees yaw Front View

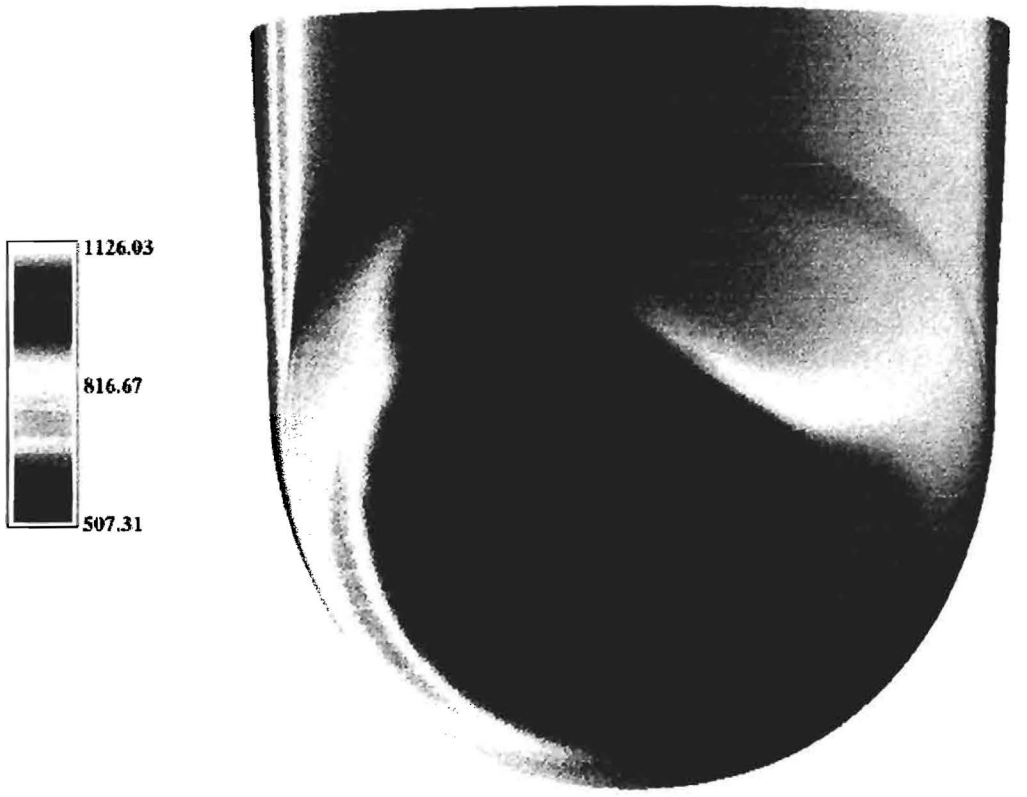

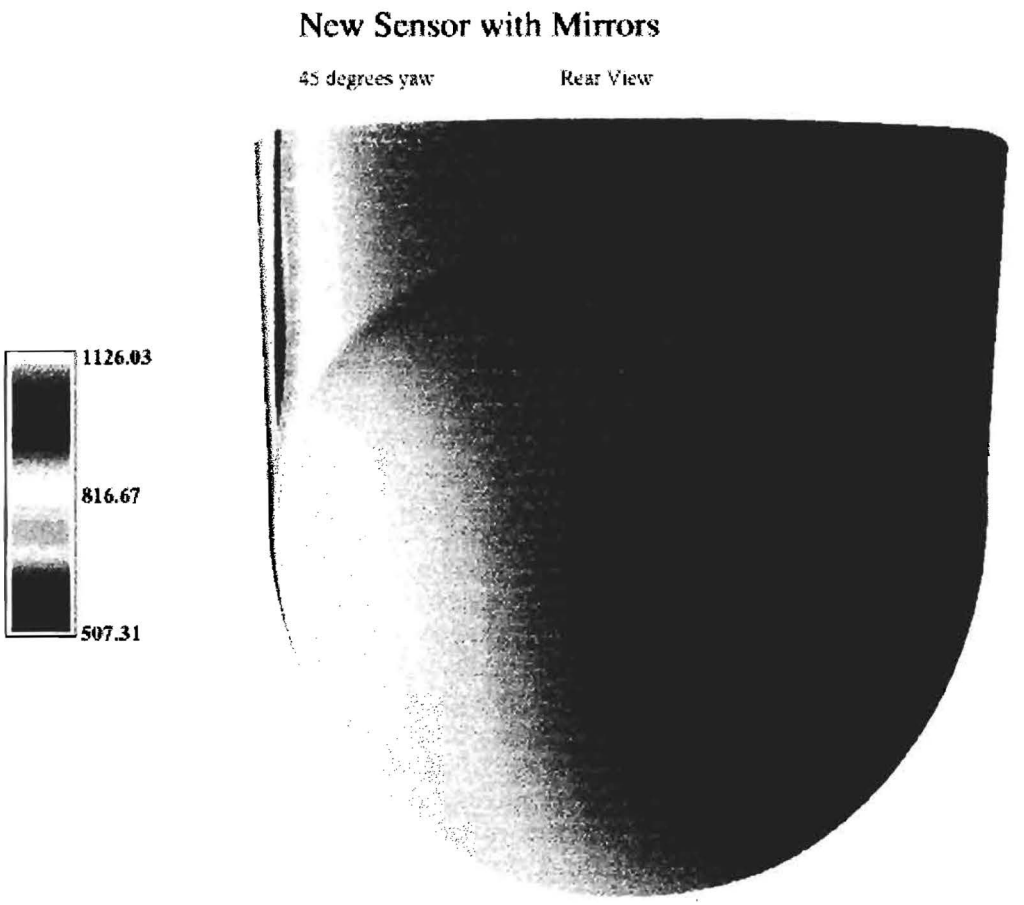

Figure 7. Surface Pressure Distribution over New Sensor with mirrors - Flat Fuselage Combination, 45 Degree yaw (Front and Rear View)

V. LOADS ACTING ON THE BASELINE AND NEW CONFIGURATIONS

In the table below, loads acting on the configuration are summarized. A total of six simulations have been completed, at the speed of 200 knots. As discussed earlier, compressibility effects were found to be minimal at this speed. As a result, the loads are proportional only to the dynamic pressure, and are not a strong function of the Mach number. The loads at a higher speed of, say, 400 knots, may therefore be found by multiplying the loads computed at 200 knots by 4, there by accounting for the four-fold increase in the dynamic pressure at the higher speed.

The pitching, rolling and yawing moments were computed about a set of Cartesian axes placed at the center of the spherical portion of the sensor. The moments at any other point on the aircraft due to the loads acting on the sensor may be easily found as:

$$\overline{M}_A = \overline{M}_B + \left(\overline{r}_A - \overline{r}_B\right) \times \overline{F}$$

where r_B represents the position of the center of the sphere, r_A represents the position of the point on the airframe where moments need to be computed, and F is the force acting on the configuration. The 'overbars' indicate that these quantities should be treated as vectors.

Configuration Configuration	Speed Speed Knots	Alpha Alpha Deg	Yaw Yaw Deg	Elevation Elevation Deg	Drag Drag Lbf	Side force Side force lbf	Lift Pitching lbf	Pitching Yawing Moment ft.lbf	Yawing Rolling Moment ft.lbf	Rolling Moment ft.lbf
Baseline	200	3	0	Not Applicable	212	0	110	54	0	0
Baseline (GASP code	200	3	0	Not Applicable	176	0	116	66.7	0	0
New Config./No mirro	200	3	0	N/A	248	0	176	26.71	0	0
New Config./No mirro	200	3	45	N/A	265	98.5	149.7	68.14	59.58	14.9
New Config./Mirrors	200	3	0	-10	236	4.842	59.58	39.93	0.18	2.7
New Cofig./Mirrors	200	3	45	-10	206	91	163	40.59	27.8	17.2
Baseline	400	3	0	N/A	848	0	440	216	0	0
Baseline (GASP code	400	3	0	N/A	704	0	464	266.8	0	0
New Config./No mirro	400	3	0	N/A	992	0	704	106.84	0	0
New Config./No mirro	400	3	45	N/A	1060	394	598.8	272.56	238.32	0.4
New Config./Mirrors	400	3	0	-10	944	19.4	238.32	159.72	0.72	7.08
New Cofig./Mirrors	400	3	45	-10	824	364	652	162.36	111.2	14.8

In the above table, the forces and moments reported are for the entire configuration, computed at the center of the sphere. The loads on the spherical portion alone have also been computed, and are reported below:

Configuration	Speed Knots	Alpha Deg	Yaw Deg	Elevation Deg	Drag Lbf	Side force lbf	Pitching lbf	Yawing Moment ft.lbf	Rolling Moment ft.lbf	Moment ft.lbf
Baseline		200	3	0 Not Applicable	142	0		1.374	0	0
Baseline (GASP code		200	3	0 Not Applicable	118	0		0.86	0	0
New Config./No mirro		200	3	0 N/A	248	0		1	0	0
New Config./No mirro		200	3	45 N/A	265	98.5		0.22	6.25	0.1
New Config./Mirrors		200	3	0 -10	149.4	2.021		10.98	2.059	1.769
New Cofig./Mirrors		200	3	45 -10	46.95	112.6		13.81	0.33	3.711
Baseline		400	3	0 N/A	568	0		5.496	0	0
Baseline (GASP code		400	3	0 N/A	472	0		3.44	0	0
New Config./No mirro		400	3	0 N/A	992	0		4	0	0
New Config./No mirro		400	3	45 N/A	1060	394		0.88	25	0.4
New Config./Mirrors		400	3	0 -10	597.6	19.4		43.92	8.236	7.08
New Cofig./Mirrors		400	3	45 -10	187.8	450.4		55.24	1.32	14.8

Note that the lift forces on the sphere alone are not meaningful, since part of the sphere is buried inside the post.

Unsteady Loads:

The flow solvers GASP and ENS3D used to study can be run in two modes - time accurate mode, or relaxation mode. In the time accurate mode, the physical phenomena are tracked in detail in time, and the computed results are a true simulation of what is observed in laboratory. Typically 10,000 or more time steps (each equal to a millisecond, or less) are needed.

In the relaxation mode, the calculations are done in pseudo-time mode. The objective here is to approach a steady state solution as quickly as possible, and not worry about the temporal path to that steady state equation. The flow solver may use short cuts (e.g. solve the flow on a very coarse grid, and use it as an initial solution on a more refined grid). The steady state solution, when one exists, is usually very reliable with this approach, and is obtained in 1000 or 2000 iterations.

In the analyses done for Lockheed Martin, the calculations were done using both these modes for the existing ("old") sensor. The calculations were typically started in the relaxation mode, and switched over to time accurate mode. The vortex shedding frequency f, which when multiplied by the sphere radius R (R= 10.5") and divided by the freestream velocity V(~ 340 ft/sec) is estimated to be around 0.2. This non-dimensional number fR/V is called Strouhal number, and usually varies between 0.2 and 0.4 for most bluff structures.

For the new sensor, we did all the calculations in the relaxation mode so that we can get the final limit cycle loads on the structure as quickly as possible. Time accurate simulations or Strouhal number estimates have not been carried out. Nevertheless, given the similarity between the old and existing probe in terms of "bluffness", it is expected that the Strouhal number and the vortex shedding frequency for both these cases to be within, say, 30% of each other.

VI. SUMMARY OF CONCLUSIONS

For the above table, the following observations are made:

i) The baseline configuration was analyzed using two computer codes, ENS3D and GASP. The drag forces are within 20% of each other, even though two entirely different computer codes were used, and the fact that the ENS3D simulation had the fuselage surface modeled in detail.
ii) The drag forces on the old and new configurations, with and without mirrors all vary between 176 and 248 lbs. In general, the new configuration has a higher drag than the baseline configuration. This may be expected, given the highly streamlined shape of the baseline configuration. The near "square" shape of the post causes extensive separation at the edges of the post, and increase the drag.
iii) Both configurations are aerodynamically classified as "bluff" and have nearly the same projected area. This explains why all the forces for the old and new configuration are within 20% of each other.
iv) The addition of mirrors make the configuration highly asymmetric, and produces a small side force (5 lbf) even where there is no cross wind.
v) The moments produced by the loads at the center of the sensor are small, below 10 ft.lbf. This indicates that one can assume that the center of pressure (or the forces) act at the center of the spherical portion of the sensor, for both the old and new configurations.
vi) The low pressures, and high velocities at the bottom of the sensor produce lift forces, which push the sensor into the fuselage. These forces were not small, and varied from 110 lbf to 176 lbf for the configurations considered. However, between the baseline configuration, and the new configuration, no significant differences were found.
vii) Calculations at an elevation angle of 45 degrees have not been completed at this writing.

In conclusion, the new configuration produces more drag than the baseline configuration. It also produces a side force due to the asymmetry of the mirrors. Other than these two effects, the two configurations produce forces and moments within 20% of each other.